Progress In Electromagnetics Research, Vol. 149, 251–273, 2014

Transformation Optics and Applications in Microwave Frequencies

Wei Xiang Jiang, Wen Xuan Tang, and Tie Jun Cui*

(*Invited Paper*)

Abstract—Modern electrical and communication technologies benefit from classical electrodynamics and electric circuits, both of which are based on the Maxwell's equations. Using the property of metric invariance in Maxwell's Equations, transformation optics has been proposed and achieves a rapid progress in the past decade. Transformation optics is a method for the conceptual design of complex electromagnetic media, offering opportunities for the control of electromagnetic waves. In this paper, we introduce the general theory of transformation optics and discuss the recent development on the transformation devices in the microwave band, such as non-singular invisibility cloak and its realization in dc circuit, three-dimensional ground-plane cloaks, flattened Luneburg lens, high-performance antennas, and high-resolution imaging lens. Some of the transformation-optics-based devices are expected to have further impact on the microwave engineering applications.

1. INTRODUCTION

Maxwell's equations are a set of partial differential equations that underlie classical electrodynamics and electric circuits [1], which form the foundation of modern electrical and communications technologies. In the past a dozen years, a rapid progress has been achieved in the subject of structured metamaterials. The rapid development of artificial metamaterials have provided many opportunities for new device design, but brought the need for tools that can provide us an efficient design for a special functionality. In 2006, Pendry et al. proposed the technique of transformation optics (TO), which fulfilled the requirement for such a tool [2]. TO is a means to visualize the interaction of a class of complex materials with electromagnetic (EM) fields in terms of a warping of space. TO has been used to design new and creative devices for conventional EM applications such as invisibility cloaks, perfect lens and flattened Luneburg lens [3–6]. For TO devices, the composing material implements a coordinate transformation for EM fields [7, 8], and the electric permittivity and magnetic permeability of the material could be derived from the methodology of TO [2, 9]. Alternatively, an optical conformal mapping method was used to design a medium that generates invisibility devices in the ray-tracing limit [10]. The invisibility cloaks were analyzed in details using geometric ray tracing method [9], and verified numerically by full-wave simulations [11] and experimentally by a two-dimensional (2D) near-field mapping configuration at the microwave frequency [12]. Inspired by the theoretical and experimental results, more researches have been conducted for cylindrical and spherical cloaks up to now [13–16]. All the basics of these numerical, analytical and experimental investigations are Maxwell's equations. Due to the possibilities of the transformation medium to control EM fields, different devices with novel functionalities have been constructed besides the invisibility cloaks, such as EM rotators [17, 18], EM concentrators [19, 20], and planar focusing antennas [21–23], etc.

Received 25 October 2014, Accepted 5 November 2014, Scheduled 10 November 2014
Invited paper for the Commemorative Collection on the 150-Year Anniversary of Maxwell's Equations.
* Corresponding author: Tie-Jun Cui (tjcui@seu.edu.cn).
The authors are with the State Key Laboratory of Millimeter Waves, Department of Radio Engineering, Southeast University, Nanjing 210096, China.

To understand the principle of TO, we imagine a fictitious space with some geometrical character that performs a desired EM phenomena, and TO yields the material property that facilitates the behavior. As an example of TO, a cloak can be designed by performing a coordinate transformation that squeezes the space from within a sphere to within a shell that has the same outer radius. Waves do not interact with or scatter from the core because it is simply not part of the transformed space. The form invariance of Maxwell's equations implies that the coordinate transformation can instead be applied to the permittivity and permeability tensors, yielding the prescription for a medium that will accomplish the desired functionality.

The organization of this paper is as follows. In Section 2, we give a brief introduction to the concept of TO and quasi-conformal mapping without proof of the property of metric invariance of Maxwell's equations. In Sections 3–8, we discuss some examples of transformation devices, such as, non-singular invisibility devices, EM concentrators, ground-plane cloak, flattened Luneburg lens, high-resolution imaging lens, and some other novel transformation devices. The summary comes in Section 9.

2. TRANSFORMATION OPTICS AND QUASI-CONFORMAL MAPPING

EM devices that perform coordinate transformations are known as transformation electromagnetic devices. The transformation devices exhibit two interesting properties. First, the optical path in the transformation device is exactly the same as that in the virtual space [8]. Second, the transformation devices are reflectionless if the metric of the transformation space in the direction normal and parallel to the interface between the transformation medium and the surrounding medium is continuous on the boundary [24]. In this section, we will give a brief description of TO principle based on the form invariance of Maxwell's equations under coordinate transformations. We here restrict our discussions to purely spatial coordinate transformations of EM fields [7–9]. In the original space, the Maxwell's equations are

$$\nabla \times \mathbf{E} + \mathrm{i}\omega\mu \cdot \mathbf{H} = 0 \tag{1}$$

$$\nabla \times \mathbf{H} - \mathrm{i}\omega\varepsilon \cdot \mathbf{E} = 0 \tag{2}$$

where both ε and μ may depend on position, that is to say, the constitutive parameters are functions of the space. Suppose that the coordinate transformation between the virtual space and the physical space is

$$\mathbf{x}' = \mathbf{x}'(\mathbf{x}). \tag{3}$$

As we know, such a transformation will give the equivalent relations because of the fact that Maxwell's equations can be written such that they are "form invariant" under coordinate transformations [25]. Under such coordinate transformations, the material parameters can be calculated. Maxwell's equations in the new coordinate system will keep the same form,

$$\nabla' \times \mathbf{E}' + \mathrm{i}\omega\mu' \cdot \mathbf{H}' = 0, \tag{4}$$

$$\nabla' \times \mathbf{H}' - \mathrm{i}\omega\epsilon' \cdot \mathbf{E}' = 0, \tag{5}$$

in the new coordinate system, the fields will be

$$\mathbf{E}'(\mathbf{x}') = \left(\Lambda^T\right)^{-1}\mathbf{E}(\mathbf{x}); \quad \mathbf{H}'(\mathbf{x}') = \left(\Lambda^T\right)^{-1}\mathbf{H}(\mathbf{x}); \tag{6}$$

and the material property will be

$$\mu'(\mathbf{x}') = \frac{\Lambda \cdot \mu(\mathbf{x}) \cdot \Lambda^T}{\det(\Lambda)}; \quad \varepsilon'(\mathbf{x}') = \frac{\Lambda \cdot \varepsilon(\mathbf{x}) \cdot \Lambda^T}{\det(\Lambda)}, \tag{7}$$

where the Jacobian transformation matrix is defined as

$$\Lambda_{ki} = \frac{\partial x'_k}{\partial x_i}; \quad \left[\Lambda^{-1}\right]_{ij} = \frac{\partial x_i}{\partial x'_j}. \tag{8}$$

For most practical devices, Equations (7) are the primary tools for the transformation-based design. Since some components of the relative permittivity and permeability of the required media are often less than 1, generally, the transformation devices are composed of inhomogeneous and anisotropic

metamaterials. In view of the difficulty to realize the full-parameter transformation devices, a published theory has suggested a technique of quasi-conformal transformation optics (QCTO), which can relax the request of the material parameters [26]. In recent years, QCTO has been widely used to design nearly-isotropic metamaterial devices, such as ground-plane cloak (or carpet cloak) [26, 27], flattened Luneburg lens [5, 6], and so on. Compared to spatial invisibility cloak, the carpet cloak does not require anisotropy of the material parameters. Furthermore, the range of permittivity and permeability is much smaller. By choosing a suitable spatial transformation, the anisotropy of carpet cloak can be minimized and the magnetic response is not necessary. As a result, to construct a carpet cloak, only isotropic dielectrics are needed. Moreover, the carpet cloak can be low-loss and broadband.

For understanding QCTO, we consider a carpet cloak design in two-dimensional (2D) problem with **E**-field polarization in z direction. Suppose that an object is placed on a perfect conductor (ground plane) and that a cloak is covered on the object, as shown in Figure 1(a). The objective is that the system is perceived as a flat ground plane by using TO. In the physical space with coordinate (x_1, y_1), we assume that the cloak is a rectangle of size (a_1, b_1) except for the cloaked region for the object. The virtual space is the configuration that an observer perceives with coordinate (x_2, y_2), shown in Figure 1(b). To design a carpet cloak mathematically, a coordinate transformation will be constructed, which maps the rectangle ($0 \le x_2 \le a_1$, $0 \le y_2 \le b_1$) in the virtual space to the cloaking region with an arbitrary boundary.

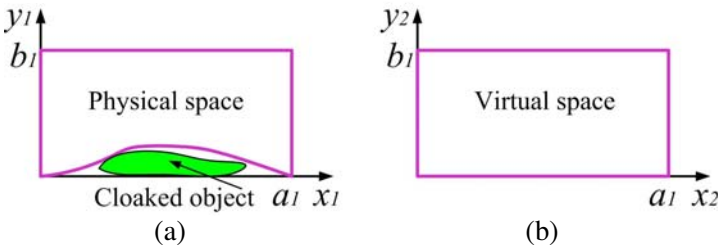

Figure 1. The principle of carpet cloak. (a) Physical space; (b) virtual space.

If the virtual space is filled with isotropic homogeneous medium of permittivity ε_{ref} and unit permeability, then corresponding physical medium induced by the coordinate transformation is given by

$$\varepsilon = \varepsilon_{ref}/|\Lambda|, \quad \mu = \Lambda \cdot \Lambda^T/|\Lambda|, \tag{9}$$

where Λ is the Jacobian matrix of the transformation. To discuss the anisotropy of the transformed medium, μ_1 and μ_2 are defined as the principal values of the permeability tensor in the physical medium, and hence the corresponding refractive indices are $n_1 = \sqrt{\mu_1 \epsilon}$ and $n_2 = \sqrt{\mu_2 \epsilon}$. An anisotropy factor α is defined to indicate the extent of anisotropy as

$$\alpha = \max(n_1/n_2,\, n_2/n_1) \tag{10}$$

If there is a very fine rectangular grid in the virtual domain with tiny cells sized $\delta \times \delta$, every such tiny square is transformed to a parallelogram in the physical domain with two sides $\xi_1\delta$ and $\xi_2\delta$. Li and Pendry's approach is to minimize the induced anisotropy by choosing a suitable coordinate transform. If the anisotropy is small enough, we can simply drop it and only keep the refractive index n. The minimal of the anisotropy occurs at the quasi-conformal mapping [26]. Every small cell in the transformed grid in the physical domain is now a rectangle with constant aspect ratio $M : m$ where M is called the conformal module of the physical domain and $m = a_1/b_1$ is the conformal module of the virtual domain, i.e.,

$$|\xi_1|/|\xi_2| = M/m, \quad \sqrt{\det(g)} = |\xi_1|\,|\xi_2|. \tag{11}$$

By substituting Equation (11) into Equation (10), we have

$$\alpha = \max\left(\frac{M}{m}, \frac{m}{M}\right)$$

independent of position. It should be noted that the quasi-conformal map approaches the conformal map [10] in the limit $M/m = 1$. In general, a quasi-conformal map is required for an unchanged topology of space without creating additional singular points in the coordinate transformation [26]. We remark that compared with the optical conformal mapping [10], the technique of quasi-conformal mapping allows the conformal module of the two domains to differ to a limited extent a crucial feature for the design. For a two-dimensional transformation, this leads to the prescription of a material with very limited anisotropy that can be well approximated by a dielectric-only response. Standard conformal grid generation methods may be used to realize such a transformation [26].

For example, to design a carpet cloak in microwave band [27], the area of a rectangle bounded by $0 \le x_2 \le 250\,\text{mm}$, $0 \le y_2 \le 96\,\text{mm}$ in the virtual space will be mapped to the same rectangle in the physical space but with the bottom boundary specified by

$$y(x) = \begin{cases} 12\cos^2\left((x-125)\pi/125\right), & 62.5 \le x \le 187.5, \\ 0, & \text{for other case.} \end{cases} \tag{12}$$

To test the effectiveness of the designed ground-plane cloak, a few experiments have been completed at different frequencies. The first experimental realization of a carpet cloak was reported at microwave frequencies in [27], in which a perturbation on a flat conducting plane was concealed. To match the complex spatial distribution of the required constitutive parameters, a metamaterial consisting of thousands of elements were constructed. We will discuss more details on carpet cloak in Section 5.

3. NON-SINGULAR CLOAK AND ITS REALIZATION IN DIRECT CURRENT

One challenge of the perfect cloak is that, on its inner boundary, some components of material parameters often require singular values, which makes the full-parameter cloak difficult to achieve even by using latest metamaterial techniques [12]. To avoid any singular values of the constitutive parameters, it was also demonstrated that an elliptical cloaking region can be crushed to a line segment using the coordinate transformation in the classical elliptical-cylindrical coordinate system [28], instead of being shrunk to a point. In this context, the relationship between classical elliptically-cylindrical coordinates (ξ, η, z) and Cartesian coordinates (x, y, z) is necessary. It is expressed as

$$x = p\cosh\xi\cos\eta, \quad y = p\sinh\xi\sin\eta, \quad z = z, \tag{13}$$

in which p is the half focus of the ellipse. In the elliptical cylindrical coordinate system, if we assume p to be constant, then isolines for ξ will be a series of elliptical cylindrical shells with the same focus value.

Similar to the circular cloak design, a spatial transformation from the elliptical region $\xi \in [0, \xi_2]$ to the annular region $\xi' \in [\xi_1, \xi_2]$ can be described mathematically as

$$\xi' = \frac{\xi_2 - \xi_1}{\xi_2}\xi + \xi_1, \quad \eta' = \eta, \quad z' = z, \tag{14}$$

where ξ_1 and ξ_2 are coordinate parameters of the inner and outer boundaries of the elliptical cloak. We denote the lengths of major axes for inner and outer shells of the cloak as a_1 and a_2. The nonlinear relationship between coordinate parameters and the lengths of major axes can be written as $\xi_i = \ln(a_i/p + \sqrt{(a_i/p)^2 - 1})$, $i = 1, 2$. We remark that the inner and outer ellipses have the same focus value $2p$. Hence the inner boundary is crushed to the line segment $2p$ using the above defined coordinate transformation.

Following the procedure stated in Section 2, one can derive the parameter tensors of the elliptical cloak. The relative electric permittivity and magnetic permeability are expressed as

$$\varepsilon'_{\xi'} = \mu'_{\xi'} = k, \tag{15}$$

$$\varepsilon'_{\eta'} = \mu'_{\eta'} = \frac{1}{k}, \tag{16}$$

$$\varepsilon'_{z'} = \mu'_{z'} = \frac{1}{k}\frac{\cosh^2\alpha - \cos^2\eta'}{\cosh^2\xi' - \cos^2\eta'}, \tag{17}$$

in which $\alpha = k(\xi' - \xi_1)$, $k = (\xi_2 - \xi_1)/\xi_2$, $\xi_1 \le \xi' \le \xi_2$ and $0 \le \eta' \le 2\pi$.

Equations (15)–(17) present full design parameters for the elliptical cloak in the classical elliptically-cylindrical coordinates. Clearly, the cloak is composed of inhomogeneous and anisotropic metamaterials with finite components for material parameter tensors. For circularly cylindrical cloaks with full parameters, singular material parameters are distributed on the whole inner boundary [14, 15], which are difficult to achieve in real applications [12]. The material parameters for the elliptical-cylindrical cloak here which crushes the cloaked object to the line segment $2p$, however, have no singularity. This fact makes it possible to realize the perfectly full-parameter cloak using man-made metamaterials.

When the focus of the ellipse becomes very small, the elliptical cloak approaches a circular cloak. In such a case, ε_ξ becomes ε_r and ε_η becomes ε_ϕ, indicating the radian and angular components of the permittivity, respectively. In consideration of the realization of cloak, we choose the shape of cloak as an exact circle while the material parameters are given by those of nearly circular cloak:

$$\varepsilon'_r = \mu'_r = k, \tag{18}$$

$$\varepsilon'_\phi = \mu'_\phi = \frac{1}{k}, \tag{19}$$

$$\varepsilon'_z = \mu'_z = \frac{\cosh^2\beta}{k\cosh^2\xi}, \tag{20}$$

in which $\beta = (\xi - \xi_1)/k$, $\xi = \ln(r/p + \sqrt{(r/p)^2 - 1})$, and $\xi_i = \ln(R_i/p + \sqrt{(R_i/p)^2 - 1})$, $i = 1$ or 2. The advantages of such invisibility cloak are that none of the parameters is singular and the changing range of all parameters is relatively small. ε_ϕ and ε_r are constants, and μ_z changes in a small range, all of which can be achieved using artificial metamaterials.

The static fields play a significant role in several applications, e.g., they are involved in photocopy machines, electrostatic spraying systems, and the electric impedance tomography. They can also be used to detect land-mines and torpedoes. As has been proved, the Laplace Equation maintains the form invariance under the coordinate transformation, and hence the TO theory applies well to static fields [2, 29]. TO employed in electrostatics is also termed as "transformation electrostatics". Recently, an ultrathin and nearly perfect dc electric cloak was proposed based on transformation in electrostatics [30], which is made of homogeneous and anisotropic conducting material. The dc invisibility cloak was composed of an ultrathin resistor-network layer with the thickness of one unit cell, which is the smallest size of artificial metamaterials. Although it is ultrathin, the dc electric cloak has nearly perfect cloaking behavior.

The coordinate transformation for design of an elliptical dc electric cloak is exactly the same as Equation (14). The conductivity tensor of the planar elliptical dc electric cloak was derived from the transformation electrostatics,

$$\sigma_{\xi'} = \frac{\xi_2 - \xi_1}{\xi_2}\sigma_0; \quad \sigma_{\eta'} = \frac{\xi_2}{\xi_2 - \xi_1}\sigma_0; \tag{21}$$

in which σ_0 is the conductivity of the homogeneous background material. The above equation clearly implies that both ξ and η components of the conductivity tensor are constant.

If the focal length $2p$ is chosen to be a very small value, the elliptical dc cloak is nearly a circular dc cloak with the outer radius R_2 and inner radius R_1. In such a case, σ_ξ becomes σ_r and σ_η becomes σ_φ, indicating the radian and angular components of the conductivity, respectively. The conductivity tensor of the nearly circular dc electric cloak is given by

$$\sigma_{r'} = k\sigma_0; \quad \sigma_{\varphi'} = \sigma_0/k; \tag{22}$$

in which $k = \frac{\xi_2 - \xi_1}{\xi_2} = \ln(R_2/R_1)/\ln(2R_2/p)$. Interestingly, this is found to be a nearly perfect dc cloak since it crushes the cloaked object to nearly a point (i.e., a very short line segment with length $2p$). From Equation (21), the material parameters of such a dc electric cloak, saying $\sigma_{r'}$ and $\sigma_{\varphi'}$, are constants, which are only related to the inner and outer radii of the cloak, and hence the material is anisotropic but homogeneous, which is difficult to be realized in nature, but can be easily emulated using the circuit theory. Using the analogy between electrically conducting materials and resistor networks, the anisotropic conductivity tensor can be implemented easily using different resistors in different directions. Particularly, when the focal length $2p$ is close to 0, k is nearly zero. Then, the radial conductivity tends to be 0, which means insulation in the radial direction; while the azimuth conductivity tends to be very

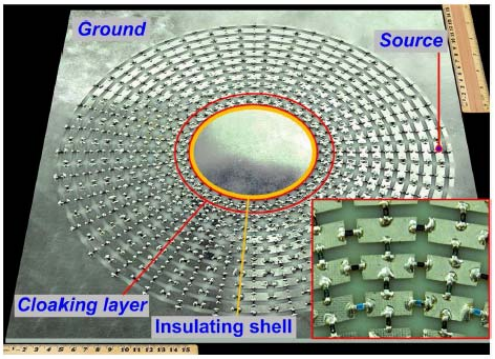

Figure 2. The photograph of fabricated single-layer dc cloak based on transformation electrostatics and resistor networks [30].

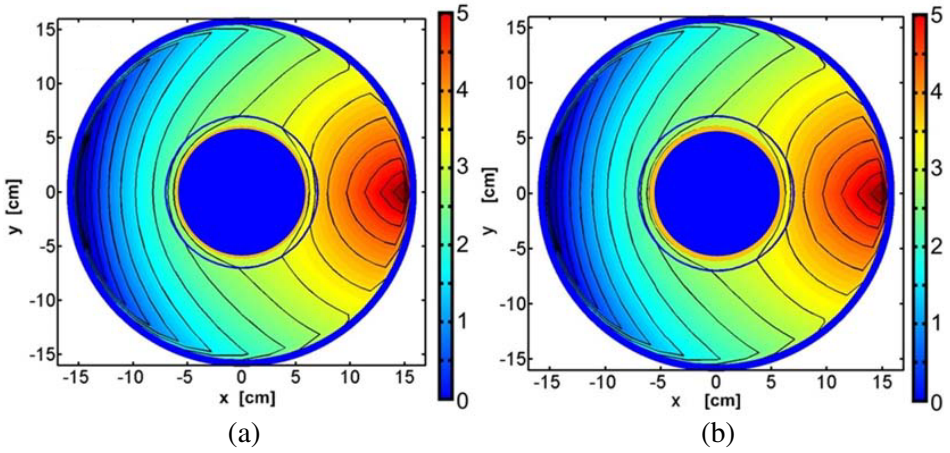

Figure 3. The simulated and measured potential distributions of the designed single-layer dc cloak. (a) Simulation result; (b) measurement result [30].

large, which means good conducting in the azimuth direction. Hence, the nearly perfect dc cloak is a combination of such two conditions and is therefore anisotropic.

In numerical simulations and experiments, an insulating shell is chosen as the inner boundary of dc electric cloak owing to the nearly zero radial conductivity. The homogeneous feature of the proposed design makes it possible to realize ultrathin dc electric cloak. The fabricated dc single-layer cloak is shown in Figure 2. In the design, the geometrical parameters are chosen as $R_1 = 5\,\text{cm}$ and $R_2 = 6\,\text{cm}$. The background material together with the dc ultrathin cloak was divided into 15×36 cells using the polar grids. The resistor network contains 10 concentric layers in the radial direction, and 36 nodes in the tangential direction, which was built on a printed circuit board (PCB) with thickness of 2 mm. The cloaked region occupies an area of 5 layers, the cloaking region employs another 1 layers, and the remaining 9 layers are background material. Figure 3 demonstrates the simulated and tested electrical-potential distributions of single-layer electric dc cloak excited by a point source, showing excellent cloaking performance. It is obvious that the potential distributions outside the cloak in both simulation and experiment are almost the same as that of the point source in homogeneous conducting material. Hence, the cloaking behavior is nearly perfect even though the thickness of dc cloak is only one layer, which is the thinnest case in discrete artificial materials.

4. EM CONCENTRATOR AND ITS EXPERIMENT IN DC

EM concentrator is a transformation device that can concentrate EM waves into a small enclosed region, which was first proposed by Rahm et al. [19]. The reduced-parameter concentrator was studied

in [31] for future practical implementation. Such a transformation device may find its applications in the energy concentration. EM concentrators with arbitrary shapes were later presented using the coordinate transformation by using non-uniform rational Bezier curves (NURBS, [32]) in representation of the geometrical boundary [20]. With the help of the NURBS curves, both the inner and outer boundaries of the concentrator can be chosen as any shapes [20]. The performance of arbitrarily-shaped concentrator verified that the fraction of plane waves could be completely focused into the inner region within the concentrator material and there are no reflected waves outside the concentrator due to the inherent impedance matching in the method of TO. Hence, the energy intensities are strongly enhanced in the inner region of the concentrator.

In order to present the transformation design, we take a circularly cylindrical EM concentrator as the example. Due to its cylindrical symmetry, it is convenient to define the transformation functions in the cylindrical coordinates (R, ϕ, z). A linear transformation for the optical design of the cylindrical concentrator is written as

$$R = \begin{cases} k_1 R', & 0 \le R' \le R_2 \\ k_2 R' - k_3 R_3, & R_2 \le R' \le R_3, \\ r, & R_3 \le R' \end{cases} \quad \phi = \phi', \quad z = z', \tag{23}$$

where the primed variables belong to the virtual space, the unprimed ones belong to the physical space, and the coefficients are $k_1 = R_1/R_2$, $k_2 = (R_3 - R_1)/(R_3 - R_2)$, $k_3 = (R_2 - R_1)/(R_3 - R_2)$. The definitions of R_1, R_2, R_3 are shown in Figure 4. The above transformation implies that the cylindrical region with radius R_2 is compressed into a smaller region with radius R_1, while the space between R_2 and R_3 is expanded to the space between R_1 and R_3. Clearly, the transformation is continuous to free space at R_3. According to Equation (7), the relative material parameters in the cylindrical coordinates can be calculated [19]. A rigorous analysis on circularly cylindrical concentrator has been discussed in [33]. However, the free-space EM concentrators have never been demonstrated experimentally since they demand highly anisotropic material parameters.

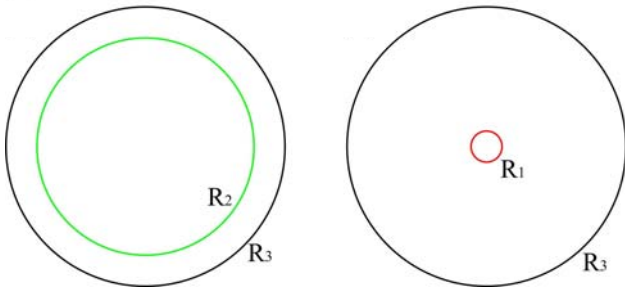

Figure 4. The principle of a circularly-cylindrical concentrator. The cylindrical region with radius R_2 is concentrated into a smaller region with radius R_1, while space between R_2 and R_3 is diluted into the space between R_1 and R_3. (a) Virtual space; (b) physical space.

A dc electric concentrator was investigated for steady current fields recently [34]. Based on the TO in electrostatics, the dc concentrator could focus electric currents into the central concentrated region and enhance the electric field and current density. Outside the concentrator, the current lines are distributed as the same as those in a homogeneous conducting material. Hence, such a dc electric concentrator has no impact on other external devices.

For the dc concentrator design, the transformation between the physical space and the virtual spaces is exactly the same as Equation (23). The electric concentrator contains two regions. In the central circular core with radius $0 \le R \le R_1$, the current density would be enhanced by R_2/R_1 times for planar source excitation by concentrating the current in region ($0 \le R' \le R_2$) into the central core; in the outer layer ($R_1 \le R \le R_3$), the current density is weakened by $(R_3 - R_1)/(R_3 - R_2)$ times for planar source excitation by diluting the current in region ($R_2 \le R' \le R_3$) into region ($R_1 \le R \le R_3$).

Then the transformed conductivity for the electric concentrator is then derived using the transformation electrostatics as

$$\overline{\sigma} = \begin{cases} \mathrm{diag}\left(1,\, 1,\, 1/k_1^2\right)\sigma_0, & 0 \le R \le R_1 \\ \mathrm{diag}\left(\sigma_R,\, 1/\sigma_R,\, k_2^2\sigma_R\right)\sigma_0, & R_1 < R \le R_3 \end{cases} \tag{24}$$

in which $\sigma_R = k_3 R_3/R + 1$. It is interesting to notice that, implied in Equation (24), the central "concentrated" region is isotropic and the conductivity is the same as that of the background material for 2D case. In the "diluted" region, the conductivity is anisotropic, whose R component is a monotonously decreasing function on radius, while the φ component is an inverse of R component.

Equation (24) shows that the realization of dc concentrator requires anisotropic and inhomogeneous conductivities, and the anisotropic conductivity tensor can be implemented using different resistors in different directions. In the experiments, two samples were fabricated. For the first sample, the background material has the conductivity of 1 S/m, which is cut into a circular region with radius of 25 cm. In the design, the inner radius was chosen as $R_1 = 5$ cm and the outer radius $R_3 = 15$ cm. The background material together with the dc concentrator is divided into 25×36 cells using the polar grids. The resistor network, which is built on PCB with thickness of 2 mm, contains 25 concentric layers in the radial direction, and 36 nodes in the tangential direction. The concentrated region of the dc concentrator occupies an area of 5 layers, the diluted region employs another 10 layers, and the remaining 10 layers are background material. For the second sample, the central concentrated region has one-layer resistors with radius $R_1 = 1$ cm and the diluted region has 10 layers of resistors, respectively. The remaining 9 layers are background material. A voltage source with 5 V magnitude was connected to the circuit network at the 24th layer for first sample and at the 19th layer for the second sample, respectively.

Figures 5(a) and 5(b) demonstrate the simulation and measurement results of a dc concentrator

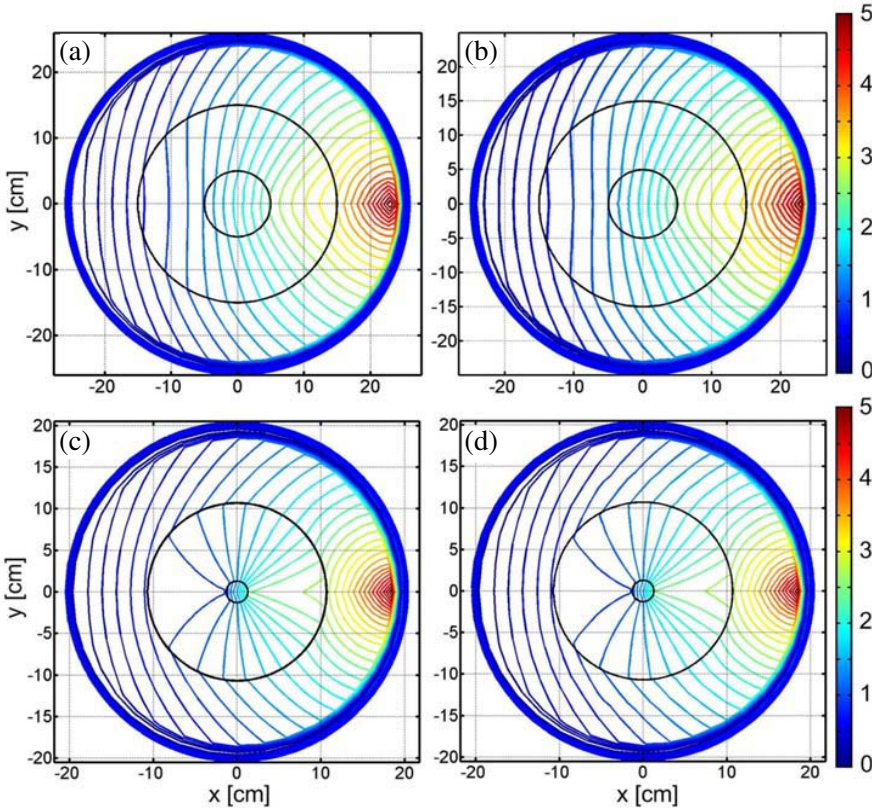

Figure 5. The equi-potential line distributions of two current concentrators. (a) The simulated result of dc concentrator with $R_1 = 5$ cm, (b) the measured result of dc concentrator with $R_1 = 5$ cm; (c) the simulated result of dc concentrator with $R_1 = 1$ cm; (d) the measured result of dc concentrator with $R_1 = 1$ cm [34].

with $R_1 = 5\,\text{cm}$, $R_2 = 10\,\text{cm}$ and $R_3 = 15\,\text{cm}$ based on the resistor network. The simulated potential distributions of the dc concentrator are shown in Figure 5(a). It is clearly observed that the potential distributions outside the concentrator keep the original equipotential lines as those in the homogeneous material, which indicates that the concentrator has no effect on any external devices. The measurement results of the dc concentrator are presented in Figure 5(b), demonstrating excellent concentrating performance. To verify such a design for a dc concentrator with a large "concentrating" factor, we fabricated the second device. Figures 5(c) and 5(d) illustrate simulation and measurement results of a dc concentrator with $R_1 = 1\,\text{cm}$, $R_2 = 10\,\text{cm}$ and $R_3 = 11\,\text{cm}$.

By comparing Figures 5(a) and 5(b), excellent agreements have been certified between the experiments and simulations, both inside and outside the concentrator. In the circuit simulations and experiments, the current density in the concentrated region has been enhanced by 1.7 times for the case of $R_1 = 5\,\text{cm}$, $R_2 = 10\,\text{cm}$ and $R_3 = 15\,\text{cm}$, and by 5.6 times for the case of $R_1 = 1\,\text{cm}$, $R_2 = 10\,\text{cm}$ and $R_3 = 11\,\text{cm}$ respectively, compared to that in the same region in the homogeneous material due to potential distribution in the logarithmic law. We remark that the enhancement factors are smaller than the theoretical predictions due to the differences of excited sources. Therefore, in the dc concentrator, the electric potential is concentrated, while the electric field and current density are enhanced. With the help of modern integrated circuit technologies, it is possible to extend such a device to the nano scale, which is expected to have potential applications in the electric impedance tomography technology, graphene, and other integrated circuits.

5. HIGH-PERFORMANCE ANTENNAS

The basic idea of wave-shape transformation comes from the fact that waves propagate perpendicular to the phase fronts in free space. Therefore, the wave shape of a non-plane wave will be changed momentarily. If a device can limit the propagation of a wave in a certain region and convert the wave shape to another style when the wave leaves, it is called wave shape transformer [42]. In topological interpretation, such a device causes the spatial deformation by mapping the points traced by the wave propagating in free space to the points within the TO device. Hence, the material parameter tensors for the device can be established by using TO theory. One can also design a transformation device that keeps wave shape. Such a transformation device keeps the phase front without changing the shape when a wave propagates through it [35].

The principle of many high-performance antennas is based on the conversion from cylindrical waves to plane waves [36]. The first work on conversion from cylindrical waves to plane waves in a short range was proposed by using the finite embedded optical transformation [37]. The principle of the conversion is shown in Figure 6(a). The radii of inner and outer circles are a and b, respectively, and the sidelength of the outer square is $2c$. The square domain is divided into four triangles and in the triangle OAB, the following transformation is constructed,

$$r' = \begin{cases} br/a, & 0 \le r \le a; \\ \dfrac{cr - bx}{(b-a)x}(r-a) + b, & a \le r \le b, \end{cases} \tag{25}$$

where (x, y) is the coordinate variables in the original space and (x', y') the corresponding variables in the transformed space, and $r = \sqrt{x^2 + y^2}$, $r' = \sqrt{x'^2 + y'^2}$. Obviously, $0 \le r' \le b$ if $0 \le r \le a$, and $b \le r'$, $x' \le c$ if $a \le r \le b$. There are two transformations in Equation (25). The first extends the space in sector $\widehat{OCD}$ to a bigger space in sector $\widehat{OA'B'}$, and the second transforms the arc $CA'B'D$ to the trapezia-like region $A'ABB'$. Hence, if cylindrical waves are excited at the origin and propagate through the domain $A'ABB'$, the phase front will change from circular to plane. The relative permittivity and permeability tensors of the materials for the single triangular domain OAB in the transformed space would be calculated by TO. By using rotation operation, the corresponding material parameter tensors for other domains can be obtained.

In the view of the realization difficulty of the above conversion method, a high-directivity lens antenna was proposed based on layered TO, which makes all layers of the lens homogeneous and uniaxially anisotropic [38]. We present the layered TO in a simple lens antenna. Such an TO device can amplify the local properties of fields in a small region to a large region. Consider a 2D structure

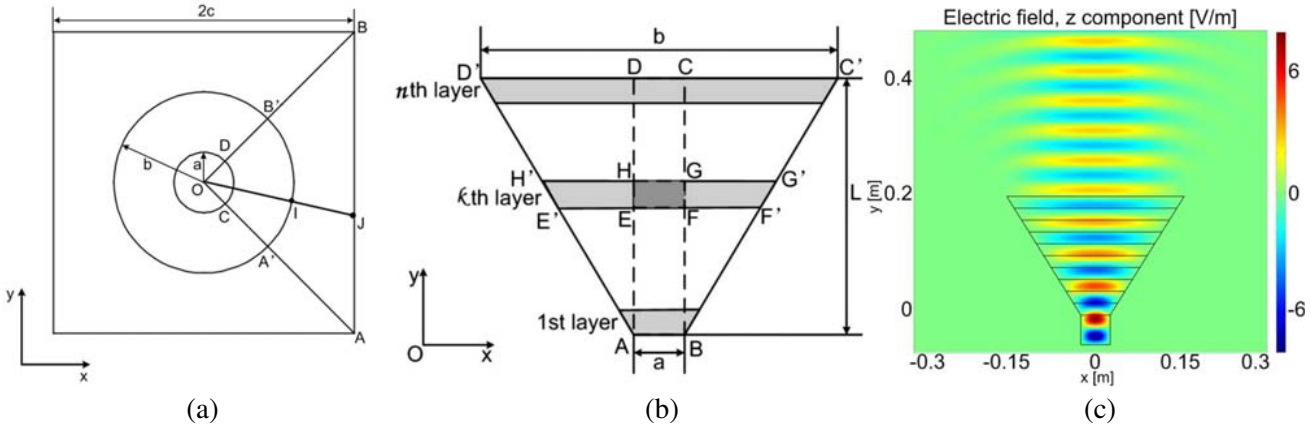

(a) (b) (c)

Figure 6. (a) The principle of cylindrical-to-plane wave-shape transformer; (b) the principle of high-directivity lens based on layered-approximate TO; (c) the simulated field distribution of layered TO lens.

in the Cartesian coordinate system, as shown in Figure 6(b), in which the virtual space is a rectangle $ABCD$ and the physical space is a trapezia $ABC'D'$. We divide the physical and virtual spaces into n layers in the same way. For the kth $(1 \leq k \leq n)$ layer, we define an elongating mapping using the following equations

$$x' = x + \frac{(k-0.5)(b-a)x}{na}, \quad y' = y, \quad z' = z \quad (1 \leq k \leq n), \tag{26}$$

where (x, y) is an arbitrary point in the virtual space and (x', y') the transformed point in the physical space. We have assumed the lengths of AB and $C'D'$ to be a and b, respectively, and the height of the trapezia $ABC'D'$ to be L. We remark that the discrete transformation implied in Equation (26) maps rectangles to wider rectangles. Therefore the actual "physical space" is actually the staircase approximation of the trapezium obtained by stacking rectangles on top of each other. At this point, the larger is the layer number n chosen, the more accurate the transformation becomes.

Hence the relative permittivity and permeability tensors of the transformation medium in the kth layer $(1 \leq k \leq n)$ are expressed as

$$\varepsilon^k_{xx} = \mu^k_{xx} = \alpha_k, \quad \varepsilon^k_{yy} = \mu^k_{yy} = 1/\alpha_k, \quad \varepsilon^k_{zz} = \mu^k_{zz} = 1/\alpha_k, \tag{27}$$

in which

$$\alpha_k = 1 + (k-0.5)(b-a)/(na). \tag{28}$$

For the TE wave incidence, the electric fields are polarized along the z axis, and only ε^k_{zz}, μ^k_{xx} and μ^k_{yy} are required in Equation (24). The dispersion relations of the transformed media remain unchanged as long as the products of $\mu^k_{xx}\varepsilon^k_{zz}$ and $\mu^k_{yy}\varepsilon^k_{zz}$ are kept the same in above equations. Hence one advantageous choice is to select

$$\mu^k_{xx} = 1, \quad \varepsilon^k_{zz} = 1, \quad \mu^k_{yy} = 1/\alpha^2_k, \quad 1 \leq k \leq n, \tag{29}$$

due to the practical reason. In this set of parameters, only μ^k_{yy} is different in each layer of the lens structure, which makes the whole structure very easy to realize. We remark that the reduced media parameters provide the same wave trajectory inside each layer of the lens antenna, and there will be no reflection for the normal incidence because of the wave-impedance matching at the upper and lower boundaries. However, for other angles of incidence there will be tiny reflections.

Similarly, the transformation design method was employed to realize substrates that can modify the emission of an embedded source [39]. With proper transformation functions, the energy radiated by a source embedded in these space variant media will be concentrated in a narrow beam [40]. Hence, the technique of optical transformations is a powerful approach for high-performance antenna designs [41]. A more general situation that converts a wave front from an arbitrary shape to another arbitrary style has

been considered in [42]. The authors proposed a general method of designing wave shape transformers. By adopting this method, a wave shape transformer that converts wave fronts with arbitrary shape and size to another arbitrary style can be constructed.

A broadband transformation optics lens has been designed and fabricated [43]. Such a lens can convert the radiation from an embedded isotropic source into any desired number of highly directive beams pointing at arbitrary directions. The impedance bandwidth of the embedded antenna was greatly enhanced by exploiting the dispersive properties of the metamaterial unit cells. The monopole with the transformation-optics lens has much better performance than the monopole without the lens in term of the gain.

6. GROUND-PLANE CLOAK

A free-space cloak based on TO always requires highly-anisotropic complex materials. For a 2D cylindrical cloak in free space, the full parameters can be greatly simplified [12]. Since the reduced parameters provide the same dispersion relationship as the full parameters for the 2D cloak, the EM waves have the same trajectory inside the cloak with a penalty of nonzero reflections. Using the reduced parameters, the first practical free-space cloak has been realized in the microwave frequency [12]. Due to the requirement of very small values of refraction index, resonant structured metamaterials have been applied, which makes the invisible cloak operate in a narrow frequency band with a relatively large loss.

The narrow bandwidth and large loss become big restriction to real applications of free-space cloaks. By using a carpet cloak based on QCTO, however, one can cause any object swept under a conducting plane to seem to disappear [26]. The great advantage of the carpet cloak is that it relaxes singular value requirement for the material parameters. The experimental validations of the carpet cloak has been achieved with low-loss and broadband metamaterials at microwave frequencies [27] and at optical frequencies recently [44, 45].

The first carpet cloak was realized with the use of non-resonant metamaterial elements, which can work in a broad bandwidth from 13 to 16 GHz while exhibiting extremely low loss. A photograph of the fabricated sample is presented in the left part of Figure 7. The entire cloak was embedded in a background material with refractive index $n_b = 1.331$. Under this condition, refractive index values for the carpet cloak ranges from $n = 1.08$ to 1.67. Because the cloak was designed to be embedded in a higher dielectric region, impedance matching layer (IML) was added to surround the entire structure, for which the index changes gradually and linearly from that of the air to that of the background index.

The elements chosen to achieve the design are all variations of the structure shown in the right part of Figure 7. By changing the dimension a, the required index range of $n = 1.08$ to 1.67 was obtained. The carpet cloak was fabricated on copper-clad PCB with FR4 substrate. The completed sample is 500 by 106 mm^2 with a height of 10 mm. The center region, 250 by 96 mm^2, corresponds to the transformed cloaking region, whereas the rest of the sample is used for dielectric embedding and impedance matching. The cloak transformation is specifically designed to compensate a perturbation introduced on the conducting surface that follows the curve $y = 12\cos^2[(x - 125)\pi/125]$ mm.

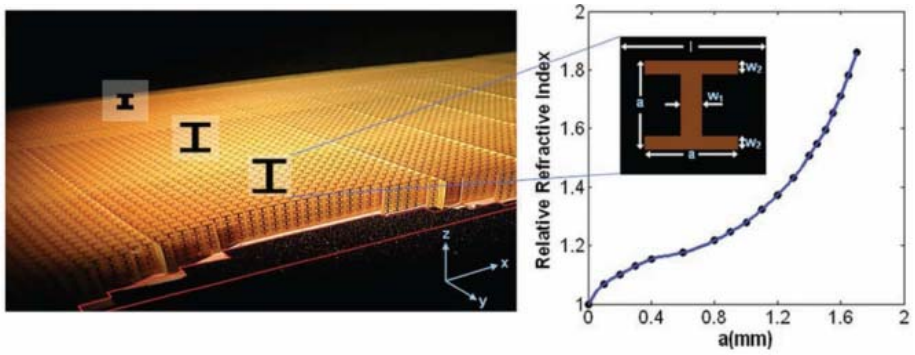

Figure 7. The photograph of the microwave carpet cloak and the metamaterial structure [27].

To verify the carpet cloak design, a near-field scanning system was used to map the electric field distribution. The planar waveguide restricts the wave polarization to transverse electric (TE). A large area field map of the scattering region, including the collimated incidence and scattered beams, is shown in Figure 8. The waves are launched into the chamber from a standard X-band coax-to-waveguide coupler and pass through a dielectric lens that produces a nearly collimated microwave beam. The beam is arbitrarily chosen to be incident on the ground plane at an angle of 40° with respect to the normal. A flat ground plane produces a nearly perfect reflection of the incident beam in Figure 8(a), whereas the presence of the perturbation produces considerable scattering, as shown in Figure 8(b). By covering the space surrounding the perturbation with the metamaterial cloaking structure, however, the reflected beam is restored, as if the ground plane were flat, shown in Figure 8(c). The gradient-index IML introduced into the design minimizes reflections at the boundaries of the cloaking region. As the carpet cloak makes use of non-resonant elements, it exhibited a large frequency range of operation. The cloaking behavior was confirmed in the range from 13 to 16 GHz.

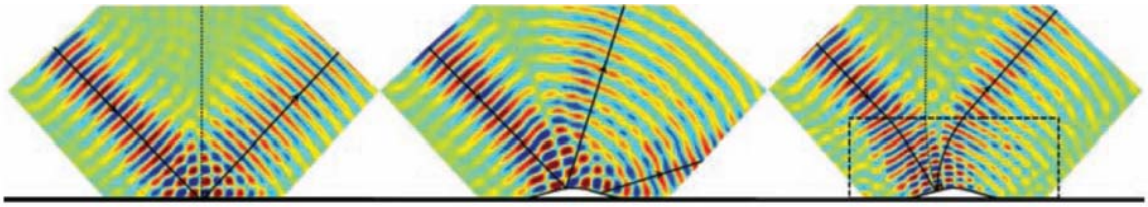

Figure 8. The measured electric fields when a collimated beam is incident on (a) a flat ground plane, (b) a perturbation, and (c) a perturbation covered by carpet cloak, respectively [27].
vskip0.1in

The non-resonant metamaterials have very low loss and operate in a broad frequency band, hence the carpet cloaks have good invisibility performance. Soon, a compact-sized carpet cloak was demonstrated experimentally in the free-space background [46]. The area ratio of the cloak to the cloaked region is as small as 7.33, which is only 11.2% of the above full carpet cloak. The simplified carpet cloak was designed in 2D with the electric fields z-polarized. The compact-sized carpet cloak covers the triangular region and makes the whole system appear as the original flat conducting plane. The shape of cloak is a rectangle with the width of 125 mm and hight of 50 mm except that the bottom boundary is partially triangularly-shaped to place the cloaked object.

The process of a compact-sized carpet cloak design contains two stages. First, following a quasi-conformal coordinate mapping, the refractive-index distribution of the cloak is computed numerically with the maximum anisotropic factor of 1.07. Secondly, the grid optimization is used by recursive division of Cartesian cells to sample the original refractive-index distribution. In such a course, the small regions near the base corners of the triangular object, where the refractive-index is smaller than 1, are treated as free space. The refractive index distribution of the final carpet cloak ranges from 1 to 1.69.

The compact-sized carpet cloak is divided to 3 by 3 mm^2 squares with non-resonant elements and fabricated on copper clad PCB with F4B substrate. Because the cell-to-cell change in dimension is minor, the impedance is matched gradually in the whole cloak over the entire measurement frequency range. The carpet has a size of $125 \times 50\,mm^2$ with a height of 12 mm. The cloaking transformation is specifically designed to compensate the triangular concealed region with the height of 13 mm and the bottom of 125 mm.

The invisible effect of the simplified carpet cloak was also validated in a near-field scanning system. The tested results demonstrated that the cloak has successfully transformed the curved surface into a flat one. The broadband properties of the compact-sized carpet cloak was verified over a wide range of frequency. The cloaking behavior was confirmed in the measurements from 10 GHz to 13 GHz. The compact-sized carpet cloak was designed based on the isotropic and non-resonant unit elements, hence the presented cloaks are broadband and low loss. The agreement between the measured field patterns and the theory provides convincing evidence that metamaterials can indeed be widely applied in practice.

The experimental demonstration of compact-sized invisibility cloaks represents a major step towards real applications of invisibility devices.

In 2010, a three-dimensional (3D) broadband carpet cloak was fabricated in the microwave frequency, which can conceal a real object located under a curved conducting sheet from all viewing angles by imitating the reflection of a flat conducting plane [47]. Following a theoretical procedure similar to that of 2D cloak, the constitutive parameter distributions was obtained for the 3D cloak. The 3D cloak was designed using inhomogeneous isotropic dielectric materials, which are realized by drilling inhomogeneous holes in layered dielectric plates. A high-gain lens antenna using non-resonant metamaterials was used as the transmitter to measure the cloaking properties of the 3D cloak.

In the description of 2D carpet cloaks, the incident waves were restricted to a single plane to which the electric field is perpendicular. Hence, only the cloak parameters in this plane were required, yielding a 2D configuration. From the optical transformation theory, the 2D carpet cloaks have good cloaking performance to all incident angles. By rotating the 2D cloak around the z axis, a 3D cylindrical carpet cloak was generated. Hence, the 3D cloak parameters can be easily obtained by rotating the available 2D cloak parameters.

The designed 3D cloak is resided in the free space, which is suitable for real cases for potential applications in the microwave frequency. The 3D carpet cloak was fabricated by drilling inhomogeneous holes in multi-layered dielectric plates, with the relative permittivity of 2.65, the standard height of F4B dielectric plate is 1 mm. Photographs of the fabricated 3D cloak sample are illustrated in Figure 9. The outline shape of the cloak is a 3D cylinder whose height and bottom radius are 51 mm and 62.5 mm, respectively. On the bottom of the cloak, the cloaked region is a cone-shaped metallic bump whose bottom radius and height are 62.5 mm and 13 mm, respectively.

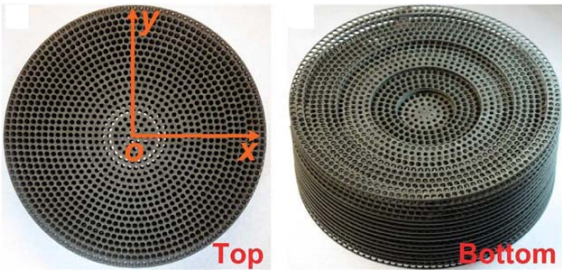

(a) (b)

Figure 9. Photograph of the fabricated 3D carpet cloak. (a) Top view; (b) bottom view [47].

To realize the drilled-hole metamaterials, two different-size unit cells are used to design the 3D cloak: $3 \times 3 \times 3\,\text{mm}^3$ and $3 \times 3 \times 1\,\text{mm}^3$, respectively. The part of the 3D cloak whose refractive indices are larger than 1.15 is fabricated using the $3 \times 3 \times 3\,\text{mm}^3$ unit cells with different-diameter holes, and the other part whose refractive indices are smaller than 1.15 is fabricated using the $3 \times 3 \times 1\,\text{mm}^3$ unit cells with different-diameter holes. The fabricated 3D cloak contains 17 layers of drilled-hole F4B plates and totally 1,310 inhomogeneous holes are drilled on a 3 mm-thick F4B dielectric plates. The drilled-hole metamaterials used in the experimental 3D cloak do have the bulk material behaviors that are expected by an ideal 3D cloak.

To verify the cloaking performance of the designed 3D carpet cloak, the scattering behaviors of objects were measured in a fully anechoic chamber. In experiments, the metamaterial transmitter has an important role. As the measured objects have relatively small sizes, the reflecting and scattering properties cannot be well captured under the illumination of conventional horn antenna in the far-field region. A gradient index metamaterial lens antenna was used as the transmitter, fro which the lens aperture is 98 mm [48]. As the metamaterial antenna can produce a narrow-beam plane wave in the near-field region, it is an excellent candidate to measure the reflecting property of the ground plane with finite size and the scattering property of the bump. The metamaterial lens was made of inhomogeneous closed-square rings (CSR), which are non-resonant metamaterial unit cells. Owing to the non-resonant nature, the lens antenna has a broadband, operating from 8 GHz to 12 GHz, covering the whole X-band. The lens antenna radiates perfect plane waves and has high gains in both E-plane and H-plane.

To observe the cloaking effect clearly, three kinds of measurements are taken in the experiments: the flat ground plane, the ground plane with cone-shaped perturbation and the ground plane with both perturbation and 3D cloak, respectively. Two polarizations of incident waves have been considered in the measurement: the incident electric field is parallel to the x-z plane (parallel polarization) and perpendicular to the x-z plane (perpendicular polarization). Such polarizations can be achieved by adjusting the feeding rectangular waveguide of the metamaterial lens. We have measured the scattered electric fields of the flat ground plane, the ground plane with perturbation and the plane with both perturbation and cloak at 9 GHz, 10 GHz and 12 GHz, respectively.

For the parallel-polarization incidence, the measured results are shown in the upper row of Figure 10. From Figure 10(a), the flat ground plane produces a single-peak reflection at the mirror-reflecting direction of the incident wave. However, the presence of the cone-shaped metallic perturbation generates considerable scattering with multi-peak reflections, as shown in Figure 10(b). When the perturbation is covered by the designed 3D cloak, however, the single-peak reflection is restored as if the ground plane were flat, as shown in Figure 10(c). Figures 10(d)–(f) illustrate the measured results for the three situations as the incident electric field is perpendicular-polarized, and similarly good cloaking performance are observed. As the 3D cloak is made of layered F4B dielectric plates, the broadband property was confirmed by the measurements in the large frequency range as expected.

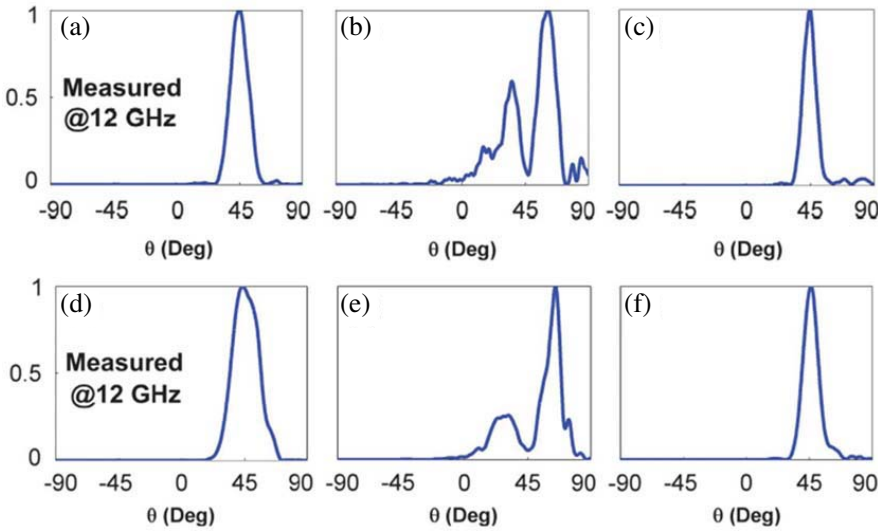

Figure 10. The measured far-field pattern of (a), (d) a flat ground plane, (b), (e) the cone-shape perturbation, (c), (f) the cone-shape perturbation with the 3D carpet cloak. The upper row is for parallel polarization and the lower row is for perpendicular polarization [47].

7. FLATTENED LUNEBURG LENS

For centuries, the conventional approach to lens design has been to grind the surfaces of a uniform material in such a manner as to sculpt the paths that rays of light follow as they transit through the interfaces. Conceptually, a more natural approach to lens design would be to vary the refractive index throughout an entire volume of space. Transformation optics can also be used to harness the flexibility of gradient index materials for imaging applications. For example, a flattened Luneburg lens, which was recently designed and experimentally demonstrated, has a field-of-view approaching 180°, and zero f-number [5]. Measurements on a metamaterial prototype of the lens illustrate the practicality of transformation optics to achieve a new class of optical devices.

It has long been known that Luneburg lens is a spherical lens with no aberrations for which the locus of focal points resides on a sphere. The fundamental problem with Luneburg lens and similar lenses, that the spherical focal locus is inherently unsuitable for standard charge-coupled devices or antenna arrays can be addressed by flattening the focal plane through the application of transformation

optics. Applying QCTO, solutions can be found that do not require the use of resonant metamaterials, implying that the resulting optic can have a large bandwidth.

The flattened Luneburg lens was designed based on QCTO, which can result in a device with identical functionality to a standard TO design, but can be implemented using isotropic materials relying only on gradients in the refractive index of the medium. The QCTO design method makes use of a set of boundary conditions that define the effect of the device, while restricting the transform inside the material. In particular, angles between the coordinate lines are approximately preserved and there is limited anisotropy of the coordinate 'squares'.

The quasi-conformal map for the flattening of a portion of a spherical lens is shown in Figure 11, which is slightly different in concept from the one carried out for the carpet cloak. The circular protrusion that follows the yellow line is mapped to a straight line that will make up the focal plane of the lens. Slipping boundary conditions are used along the yellow line in the quasi-conformal relaxation procedure. The transformation is ended with a Dirichlet boundary condition at the red line.

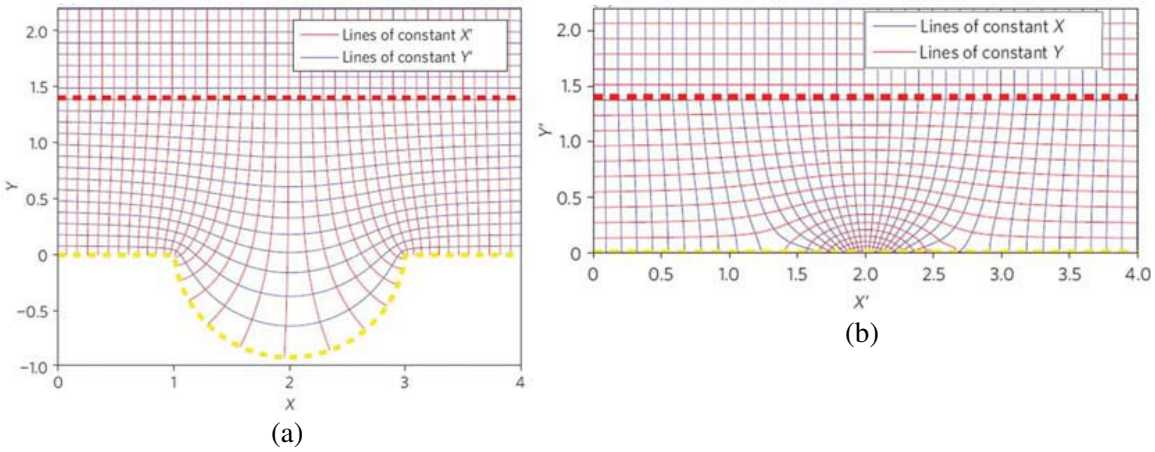

Figure 11. The principle of the flattened Luneburg lens. (a) The virtual space; (b) the physical space [5].

The lens fabricated to demonstrate the flattened Luneburg design was built to work in a parallel-plate waveguide. The index profile for the design had to be adjusted to remove regions of $n < 1$. The index was set to 1 in any region where it had previously been less than 1. An index range of 1.08 to 4.1 was used in the implementation of this design. The index profile was achieved by patterning copper strips on an FR4 substrate. The copper strips act as polarizable inclusions in the medium, increasing the overall polarizability of the material. These strips are not resonant in the frequency range of operation for the lens, and simulations indicate that the dissipative loss of these metamaterial cells is essentially equal to that of the substrate material. To achieve the requisite index range, the lens was divided into two regions. The first region contained materials with an index between 1 and 2. The second one had an index range from 2 to 4.1 and was composed of 0.22-mm-thick FR4 and copper strips laid directly on top of one another. This compact design allowed the index to be brought to over 4 without using resonant particles or introducing excessive spatial dispersion, both of which would have imposed bandwidth limitations. In the band from 7 to 15 GHz the index changes by less than 10% in the region with the largest dispersion, and less than 3% in most of the device.

The lens was tested using a dielectric waveguide to apply a source to different positions along the back surface of the lens. This set-up allowed the effects of the impedance mismatching on the back of the lens to be minimized. The lens produces approximately plane waves propagating in different directions as the position of the source is varied, extending to extreme angles approaching the horizon. The resulting field profiles are shown in Figure 12. Note that the material response is broadband. The effect of the lens does not qualitatively change between 7 and 15 GHz, the frequency range of the measurement capabilities.

The designed lens has a flat focal locus, making it usable with standard imaging arrays.

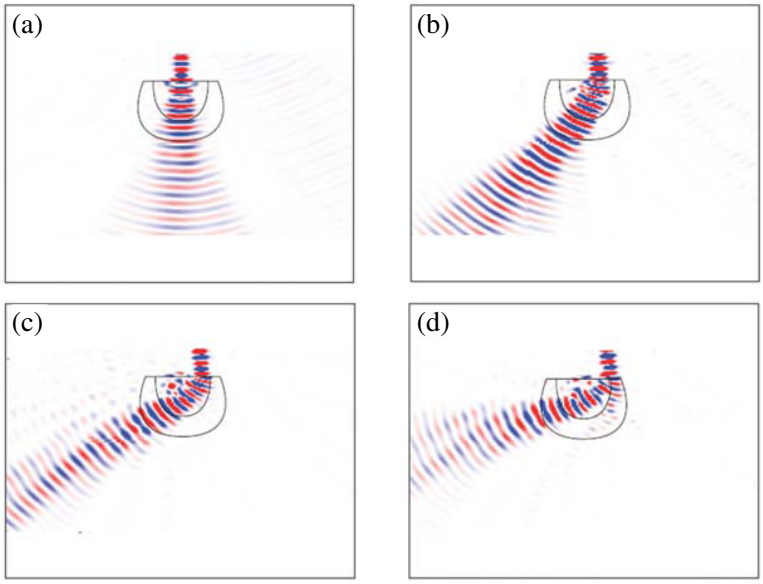

Figure 12. The measured results of the flattened Luneburg lens. (a) Beam is directed to 0°; (b) beam is directed to 35°; (c) beam is directed to 50°; (d) beam is directed to 70° [5].

Furthermore, no resonant particles were required in the fabrication of the lens, resulting in a device that is broadband and shows limited loss. The above demonstration was only limited to a 2D form with the TE mode. About one year later, a three-dimensional (3D) version of the flattened Luneburg lens in the microwave frequency band was reported [6]. The 3D lens was fabricated with multilayered dielectric plates by drilling inhomogeneous holes and had excellent performance for different polarizations over a broad frequency band from 12.4 to 18 GHz.

To generate the refractive index distribution of the 3D Luneburg-based lens, the authors rotated the 2D profile along the z axis. The 3D lens has a height of $h = 104\,\text{mm}$ and a maximum aperture of $d = 108\,\text{mm}$. This is an approximate transformation-optics lens. When a source is placed at different positions on the flattened focal surface, the lens will radiate perfectly planar wavefronts at different angles on the planes containing the optical axis. On the planes not containing the optical axis, the planar wavefronts will have some distortions.

The 3D lens is composed of non-resonant metamaterials, which are fabricated with multilayered dielectric plates, and each layer is drilled by different inhomogeneous holes to realize the 3D distribution of refractive indices. Figure 13 illustrates the photograph of the final sample of the 3D lens. Two kinds of dielectric plates are involved in the lens' realization: the FR4 dielectric, which has a large relative permittivity of 4.4, and the F4B dielectric, which has a small relative permittivity of 2.65. The 3D TO lens was designed to work in the Ku-band, and three kinds of unit cells were chosen as building blocks of metamaterials to achieve the required distribution of refractive index. The three kinds of unit cells are $2 \times 2 \times 1\,\text{mm}^3$ and $2 \times 2 \times 2\,\text{mm}^3$ F4B dielectric blocks, and $2 \times 2 \times 2\,\text{mm}^3$ FR4 dielectric blocks. The continuous variation of the refractive index can be obtained by changing the diameter of the drilling hole in the unit cell.

To verify the actual performance of the 3D flattened Luneburg lens, both near and far electric fields produced by the lens was measured when a feeding source is placed at different positions on the flattened focal surface. In the near-field measurement setup, a coaxial probe was placed in front of the lens to detect the electric fields in the near-field region. The test region is a $198 \times 198\,\text{mm}^2$ square area outside the 3D lens, which is shifted when the feeding source is placed at different locations. A Ku-band coax-to-waveguide device with an aperture size of $16 \times 8\,\text{mm}^2$ was used to feed the antenna. The detection probe was fixed, and the 3D lens was controlled by an electronic motor under an aluminium plate that moves automatically to measure the near fields continuously. It is noted that the detection probe should be parallel to the polarization direction of electric fields to get the best measurement results. Different

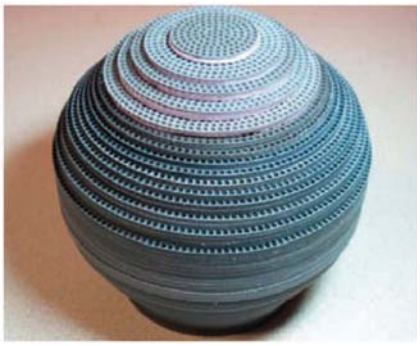

Figure 13. Photograph of the fabricated 3D flattened Luneburg lens [6].

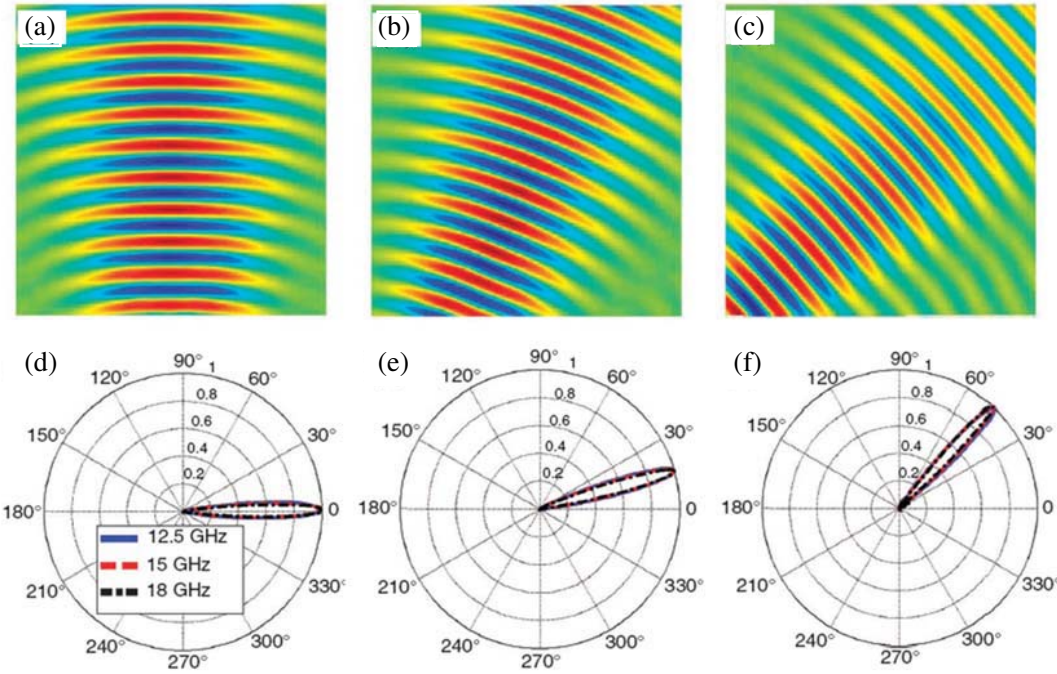

Figure 14. The measured near-field distributions and far-field patterns of the 3D flattened Luneburg lens. (a), (d) The feed is located at the lens center; (b), (e) the lens is 10 mm off the lens center; (c), (f) the lens is 30 mm off the lens center. The upper row shows the near field distribution, and the lower row shows the far-field patterns [6].

polarizations in the measurement can be considered by adjusting the feeding coax-to-waveguide device.

The measurement results of the near electric fields under vertical polarization are illustrated in Figure 14, in which three typical source positions are chosen on the focal plane: the feed is located at the lens center, 10 mm off the lens center and 30 mm off the lens center. When the feed is located at the center of the focal plane, the 3D lens generates very good planar wavefronts in the z direction (Figure 14(a)); when the source is 10 mm off the center, the 3D lens radiates good plane waves propagating in the angle of 20° off the z direction (Figure 14(b)); as the source is 30 mm off the center, the plane waves propagate in the direction of 50° off the z axis (Figure 14(c)). As the 3D lens was fabricated using multilayer isotropic dielectric plates by drilling inhomogeneous holes, the lens works in a broad frequency band from 12.4 to 18 GHz. From the above measurement results, we clearly observe that the radiation direction can be controlled in a large angle range by moving the feeding source on the flattened focal surface in the whole Ku-band.

The 3D lens was also measured in the anechoic chamber to observe the far-field radiations for both horizontal and vertical polarizations. The measured far-field radiation patterns are illustrated in

Figures 14(d)–(f), with different feeding positions on the flattened focal surface at different frequencies. The broadband property of the 3D lens is well kept in the far-field radiations, which is valid for both horizontal and vertical polarizations. Apparently, it has very good overall performance. As a planar array of feeding sources is placed on the flattened focal surface, the radiation beam of the 3D lens will be scanned in a range of 50° with respect to the normal direction (z axis).

The proposed 3D lens is more advantageous with zero focal distance, flattened focal surface and ability to generate radiation beams at extremely large angles when compared to the conventional 3D Luneburg lens. When the feeding source is located near the center of the focal plane, very good planar wavefronts are also observed on all planes not containing the optical axis. When the feeding source is far away from the center and becomes close to the edge of the focal plane, the planar wavefronts are well kept on planes not containing but close to the optical axis. Only on planes far away from the optical axis do the wavefronts have severe distortions. Such a lens can be used for beam scanning in a range of 50°, realizing a high-performance beam-scanning antenna. More generally, it is expected to be useful in telecommunications or radar applications where a wide field of view and high gain are needed.

8. HIGH-RESOLUTION IMAGING

The resolution of a conventional optical microscope is constrained to about one half wavelength due to the loss of high spatial frequency information carried in the evanescent waves [49]. Based on TO and the development of metamaterials, there has been an intensive effort to break the Abbe diffraction limit the past decade [50, 52, 53]. Perfect lens, engineered from a slab of ideal negative-refraction medium, has promised to achieve perfect image by magnifying the evanescent waves [50, 51]. For practical realization, a simplified perfect lens, i.e., the superlens, was experimentally demonstrated using a thin slab of silver [54] or SiC [55].

However, relying on the coupling between evanescent waves and surface plasmons, it is very challenging to realize low-loss superlens or hyperlens operating in broadband due to the involvement of negative-index metamaterials or metals. Moreover, the "nearsighted" superlenses cannot be directly used to replace the traditional optical microscope [56]. To project a near-field image into the far-field region, a far-field superlens (FSL), made of slab superlens with periodic corrugations, was presented later to convert evanescent waves partly into propagating waves [57]. To achieve the high resolution imaging in the far-field region more efficiently, hyperlenses which allow magnification of deep subwavelength scale objects were proposed by using hyperbolic metamaterials [58–60]. Soon after, cylindrical hyperlenses [61] and spherical hyperlens [62] were experimentally demonstrated with a curved periodic stack of metal-dielectric materials. In fact, based on TO, both superlens and hyperlens can be precisely designed [52, 53]. To avoid the absorption and narrowband properties, a broadband magnifying lens was introduced and analyzed theoretically in visible light [63] and verified experimentally in broad microwave band [64].

An impedance-matched magnifying lens, which is made of inhomogeneous isotropic dielectrics based on an simplification from TO, was fabricated to provide far-field subwavelength imaging. This magnifying lens may also be perceived as a modified solid immersion lens (MSIL) operating in microwaves. The lens is fabricated with multilayered dielectric plates with drilled air holes. The far-field high resolution imaging of such lens has been experimentally demonstrated in a broadband of gigahertz frequencies. Benefitting from the low-loss and broadband properties of the all-dielectric metamaterial, the experimental results show excellent super-resolution performance from 7 to 10 GHz. The MSIL is capable of magnifying the sub-wavelength space between two objects, and producing a magnified image at the far field, where the two objects could be distinguished by conventional imaging system.

The principle of TO-based MSIL is shown in Figures 15(a) and 15(b), in which a two-fold transformation needs to be carried out for the design. The physical and virtual spaces are denoted with (R, φ, z) and (R', φ', z'), respectively. First, a circular region ($R' \leq b - \delta$) in the virtual space is compressed into region I ($R \leq a$) in physical space. Second, an annular region ($b - \delta \leq R' \leq b$) in the virtual space is stretched into region II ($a < R \leq b$) in the physical space. Using TO procedure, the closed-form expressions of material parameters was obtained for the MSIL. In the case of two dimensions under the TE polarization and letting $\delta \to 0$, the derived refractive index of the MSIL is anisotropic, which is very difficult for realization. By comparing the far-field patterns for the anisotropic materials

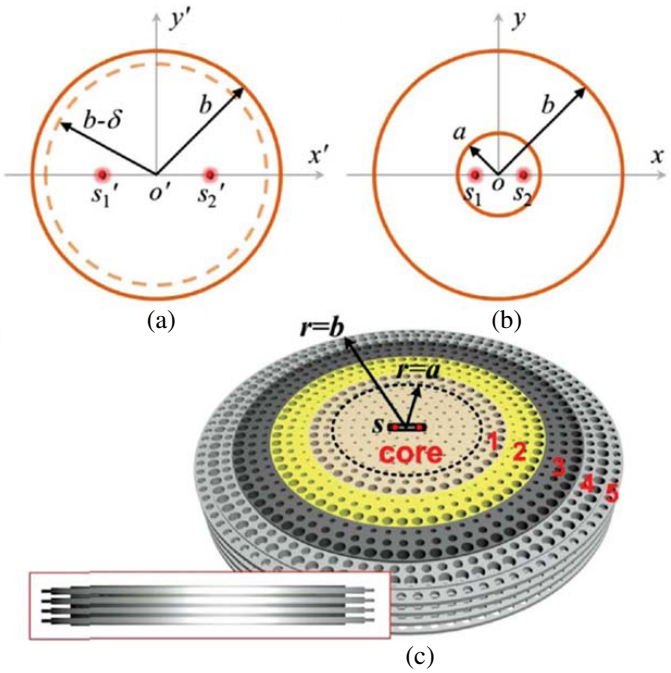

Figure 15. The principle of the magnifying lens. (a) The virtual space; (b) the physical space; (c) illustration of the fabricated magnifying lens [64].

and the simplified isotropic materials, finally an isotropic MSIL was obtained

$$n(r) = \begin{cases} b/a & R \leq a \\ b/R & a < R \leq b. \end{cases} \tag{30}$$

Obviously, the material profile in Equation (30) can be generated by full dielectrics with the broadband performance. The MSIL is schematically illustrated in Figure 15(c), which includes two parts: region I is the core region, while region II is physically the impedance-matching layer. The role of the core region is to generate subwavelength propagation mode and the matching layer effectively transmits the sub-resolution information into the free-space propagating waves. Equation (30) implies that the refractive index of the matching layer changes gradually from that of the core to that of free space. Compared to the well-studied SILs [65], the MSIL here will transmit the signature of the sources more efficiently to the far field due to the impedance-matching layer. The sources to be imaged are embedded in the MSIL by engraving a small air opening in the core center.

The material parameters of the MSIL are nonmagnetic, isotropic and inhomogeneous, which can be realized by non-resonant metamaterials and was fabricated by drilling spatially inhomogeneous air holes. The MSIL works in a broadband from 7 to 10 GHz, and five kinds of unit cells are chosen as the building blocks of the metamaterials to realize the required distribution of refractive index. In real fabrications, the MSIL is composed of four layers of the same structures, in which each layer is composed of the core region and the matching region. In experiments, a near-field scanning system is employed to measure the electric-field distributions. The distance of two small-distance sources is 7.5 mm, and the distance of two large-distance sources is 22.5 mm. The small-distance source was embedded into a slot in the center of MSIL. With this slot, the source will be immersed in the magnifying lens. Due to the symmetry of the MSIL and the feeding source, only half region is mapped.

To validate the designed impedance-matching magnifying lens experimentally, the fabricated sample with the radius of core region $a = 18$ mm, the outer radius $b = 54$ mm, and the small distance of the sources $d = 7.5$ mm, was measured in broadband from 7 to 10 GHz. Note that, at 10 GHz, the small distance (d) of two sources is 0.25 wavelength and the large distance ($3d$) is 0.75 wavelength; while at 7 GHz, the small distance is 0.175 wavelength and the large distance is 0.525 wavelength. Figure 16 illustrates the measured results of two small-distance and two large-distance sources, respectively. Figure 16(a) shows the near-field distributions of two small-distance sources without MSIL at 8 GHz.

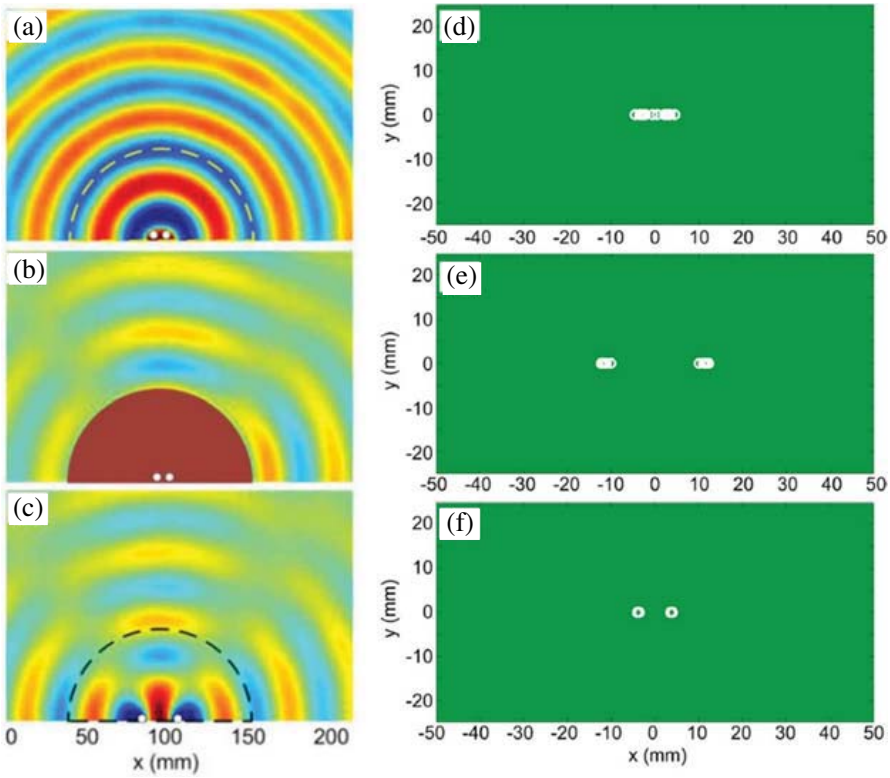

Figure 16. The measured near-fields of (a) two small-distance sources in free space; (b) two small-distance sources in MSIL; (c) two large-distance sources in free space; the inversion positions of (d) two small-distance sources in free space; (e) two small-distance sources in MSIL; (f) two large-distance sources in free space [64].

In this case, the distance of two sources is much smaller than the diffraction limit, and hence the near field is very similar to that of a single source. That is to say, the sources are very difficult to be distinguished. When the two small-distance sources are embedded in the MSIL, however, the field distributions are changed to nearly the same as those of two sources at large distance in free space, as demonstrated in Figures 16(b) and 16(c), hence, the two sources can be evidently distinguished. For practical applications, it is important to be able to deduce the configuration of the sources embedded in the MSIL based on the recorded far-field radiation patterns. Therefor, an inversion scheme has been developed to determine the positions of sources from far fields. The results are demonstrated in Figures 16(d)–(f). For the two 7.5 mm-distance sources in free space, the retrieved locations of two sources are difficult to be distinguished, as shown in Figure 16(d). However, when such two sources are placed in the graded magnifying lens, their physical positions can be clearly identified, as displayed in Figure 16(e). For the two sources with 22.5 mm separation in free space, the retrieved positions are distinctly perceived (see Figure 16(f)) since they are beyond the diffraction limit.

Such a MSIL was fabricated in microwave frequencies using the full-dielectric metamaterials. The experimental results have verified the super-resolution performance of the dielectric MSIL in broadband from 7 to 10 GHz. Owing to the low loss and broadband properties, this MSIL can be used to far-field imaging with high resolution that could be captured directly by a conventional microwave imaging device. This mechanism may also find unique potentials in far-field high resolution optical imaging. The proposed operation with high resolution may open new avenues towards real-time imaging systems across a wide spectrum of light.

9. SUMMARY

We have reviewed the theory of transformation optics which is based on Maxwell's equations and discussed several categories of TO devices that came forth in the past years. TO enables the redirect

manipulation of EM waves, and therefore offers a powerful tool for design of novel and complicated devices. For example, invisibility, previously thought purely in the realms of science fiction, now can be realized by metamaterials with the help of the theory discussed here. We believe that TO design will prove to be a more powerful methodology. Together with advancing metamaterial technology, it should lead to the realization of devices that would be very difficult to fabricate in any other way. Transformation optics is expected to have further impact on the development of electromagnetics and microwave engineerings.

ACKNOWLEDGMENT

This work was supported in part by the National Natural Science Foundation of China under Grant Nos. 61171024, 61171026, 61401089 and 61138001, in part by the National High Tech (863) Projects under Grant Nos. 2011AA010202 and 2012AA030402, in part by the 111 Project under Grant No. 111-2-05, and in part by the Natural Science Foundation of the Jiangsu Province BK2012019.

REFERENCES

1. Maxwell, J. C., "A dynamical theory of the electromagnetic field," *Philosophical Transactions of the Royal Society of London*, Vol. 155, 459–512, 1865.
2. Pendry, J. B., D. Schurig, and D. R. Smith, "Controlling electromagnetic fields," *Science*, Vol. 312, 1780, 2006.
3. Pendry, J. B., "Perfect cylindrical lenses," *Opt. Express*, Vol. 11, 755, 2003.
4. Yan, M., W. Yan, and M. Qiu, "Cylindrical superlens by a coordinate transformation," *Phys. Rev. B*, Vol. 78, 125113, 2008.
5. Kundtz, N. and D. R. Smith, "Extreme-angle broadband metamaterial lens," *Nat. Mat.*, Vol. 9, 129–132, 2010.
6. Ma, H. F. and T. J. Cui, "Three-dimensional broadband and broad-angle transformation-optics lens," *Nat. Comm.*, Vol. 1, 124, 2010.
7. Leonhardt, U. and T. G. Philbin, "General relativity in electrical engineering," *New J. Phys.*, Vol. 8, 247, 2006.
8. Leonhardt, U. and T. G. Philbin, "Transformation optics and the geometry of light," *Prog. Opt.*, Vol. 53, 69–152, 2009.
9. Schurig, D., J. B. Pendry, and D. R. Smith, "Calculation of material properties and ray tracing in transformation media," *Opt. Express*, Vol. 14, 9704, 2006.
10. Leonhardt, U., "Optical conformal mapping," *Science*, Vol. 312, 1777, 2006.
11. Cummer, S. A., B.-I. Popa, D. Schurig, D. R. Smith, and J. B. Pendry, "Full-wave simulations of electromagnetic cloaking structures," *Phys. Rev. E*, Vol. 74, 036621, 2006.
12. Schurig, D., J. J. Mock, B. J. Justice, S. A. Cummer, J. B. Pendry, A. F. Starr, and D. R. Smith, "Metamaterial electromagnetic cloak at microwave frequencies," *Science*, Vol. 314, 977, 2006.
13. Cai, W., U. K. Chettiar, A. V. Kildishev, and V. M. Shalaev, "Optical cloaking with metamaterials," *Nat. Photon.*, Vol. 1, 224, 2007.
14. Chen, H., B.-I. Wu, B. Zhang, and J. A. Kong, "Electromagnetic wave interactions with a metamaterial cloak," *Phys. Rev. Lett.*, Vol. 99, 063903, 2007.
15. Ruan, Z., M. Yan, C. W. Neff, and M. Qiu, "Ideal cylindrical cloak: Perfect but sensitive to tiny perturbations," *Phys. Rev. Lett.*, Vol. 99, 113903, 2007.
16. Yan, M., Z. Ruan, and M. Qiu, "Cylindrical invisibility cloak with simplified material parameters is inherently visible," *Phys. Rev. Lett.*, Vol. 99, 233901, 2007.
17. Chen, H. and C. T. Chan, "Transformation media that rotate electromagnetic fields," *Appl. Phys. Lett.*, Vol. 90, 241105, 2007.
18. Chen, H., B. Hou, S. Chen, X. Ao, W. Wen, and C. T. Chan, "Design and experimental realization of a broadband transformation media field rotator at microwave frequencies," *Phys. Rev. Lett.*, Vol. 102, 183903, 2009.

19. Rahm, M., D. Schurig, D. A. Roberts, S. A. Cummer, D. R. Smith, and J. B. Pendry, "Design of electromagnetic cloaks and concentrators using form-invariant coordinate transformations of Maxwell's equations," *Photo. Nano. Fund. Appl.*, Vol. 6, 87, 2008.
20. Jiang, W. X., T. J. Cui, Q. Cheng, J. Y. Chin, X. M. Yang, R. Liu, and D. R. Smith, "Design of arbitrarily shaped concentrators based on conformally optical transformation of nonuniform rational B-spline surfaces," *Appl. Phys. Lett.*, Vol. 92, 264101, 2008.
21. Kong, F., B.-I. Wu, J. A. Kong, J. Huangfu, S. Xi, and H. Chen, "Planar focusing antenna design by using coordinate transformation technology," *Appl. Phys. Lett.*, Vol. 91, 253509, 2007.
22. Schurig, D., J. B. Pendry, and D. R. Smith, "Transformation-designed optical elements," *Opt. Express*, Vol. 15, 14772, 2007.
23. Kwon, D.-H. and D. H. Werner, "Transformation optical designs for wave collimators, flat lenses and right-angle bends," *New J. Phys.*, Vol. 10, 115023, 2008.
24. Rahm, M., S. A. Cummer, D. Schurig, J. B. Pendry, and D. R. Smith, "Optical design of reflectionless complex media by finite embedded coordinate transformations," *Phys. Rev. Lett.*, Vol. 100, 063903, 2008.
25. Moon, P. and D. E. Spencer, *Field Thoery Handbook*, Springer-Verlag, Berlin, 1961.
26. Li, J. and J. B. Pendry, "Hiding under the carpet: A new strategy for cloaking," *Phys. Rev. Lett.*, Vol. 101, 203901, 2008.
27. Liu, R., C. Ji, J. J. Mock, J. Y. Chin, T. J. Cui, and D. R. Smith, "Broadband ground-plane cloak," *Science*, Vol. 323, 366, 2009.
28. Jiang, W. X., T. J. Cui, X. M. Yang, Q. Cheng, R. Liu, and D. R. Smith, "Invisibility cloak without singularity," *Appl. Phys. Lett.*, Vol. 93, 194102, 2008.
29. Yang, F., Z. L. Mei, T. Y. Jin, and T. J. Cui, "dc electric invisibility cloak," *Phys. Rev. Lett.*, Vol. 109, 053902, 2012.
30. Jiang, W. X., C. Y. Luo, Z. L. Mei, and T. J. Cui, "An ultrathin but nearly perfect direct current electric cloak," *Appl. Phys. Lett.*, Vol. 102, 014102, 2013.
31. Wang, W., L. Lin, J. Ma, C. Wang, J. Cui, and C. Du, "Electromagnetic concentrators with reduced material parameters based on coordinate transformation," *Opt. Express*, Vol. 16, 11431, 2008.
32. Piegl, L. and W. Tiller, *The NURBS Book*, 2nd Edition, Springer-Verlag, New York, 1996.
33. Luo, Y., H. Chen, J. Zhang, L. Ran, and J. Kong, "Design and analytical full-wave validation of the invisibility cloaks, concentrators, and field rotators created with a general class of transformations," *Phys. Rev. B*, Vol. 77, 125127, 2008.
34. Jiang, W. X., C. Y. Luo, H. F. Ma, Z. L. Mei, and T. J. Cui, "Enhancement of current density by dc electric concentrator," *Scientific Reports*, Vol. 2, 956, 2012.
35. Ma, H., S. Qu, Z. Xu, and J. Wang, "Wave-shape-keeping media," *Opt. Lett.*, Vol. 34, 127–129, 2009.
36. Kraus, J. D. and R. J. Marhefka, *Antennas for All Applications*, 3rd Edition, McGraw-Hill, New York, 2002.
37. Jiang, W. X., T. J. Cui, H. F. Ma, X. Y. Zhou, and Q. Cheng, "Cylindrical-to-plane-wave conversion via embedded optical transformation," *Appl. Phys. Lett.*, Vol. 92, 261903, 2008.
38. Jiang, W. X., T. J. Cui, H. F. Ma, X. M. Yang, and Q. Cheng, "Layered high-gain lens antennas via discrete optical transformation," *Appl. Phys. Lett.*, Vol. 93, 221906, 2008.
39. Zhang, J. J., Y. Luo, S. Xi, H. Chen, L.-X. Ran, B.-I. Wu, and J. A. Kong, "Directive emission obtained by coordinate transformation," *Progress In Electromagnetics Research*, Vol. 81, 437–446, 2008.
40. Kundtz, N., D. A. Roberts, J. Allen, S. Cummer, and D. R. Smith, "Optical source transformations," *Opt. Express*, Vol. 16, 21215, 2008.
41. Zhang, J., Y. Luo, H. Chen, and B.-I. Wu, "Manipulating the directivity of antennas with metamaterial," *Opt. Express*, Vol. 16, 10962, 2008.
42. Ma, H., S. Qu, Z. Xu, and J. Wang, "General method for designing wave shape transformers,"

Opt. Express, Vol. 16, 22072–22082, 2008.

43. Jiang, Z. H., M. D. Gregory, and D. H. Werner, "Experimental demonstration of a broadband transformation optics lens for highly directive multibeam emission," *Phys. Rev. B*, Vol. 84, 165111, 2009.
44. Gabrielli, L. H., J. Cardenas, C. B. Poitras, and M. Lipson, "Silicon nanostructure cloak operating at optical frequencies," *Nat. Photon.*, Vol. 3, 461, 2009.
45. Valentine, J., J. Li, T. Zentgraf, G. Bartal, and X. Zhang, "An optical cloak made of dielectrics," *Nat. Materials*, Vol. 8, 568, 2009.
46. Ma, H. F., W. X. Jiang, X. M. Yang, X. Y. Zhou, and T. J. Cui, "Compact-sized and broadband carpet cloak and free-space cloak," *Opt. Express*, Vol. 17, 19947, 2009.
47. Ma, H. F. and T. J. Cui, "Three-dimensional broadband ground-plane cloak made of metamaterials," *Nat. Comm.*, Vol. 1, 21, 2010.
48. Chen, X., H. F. Ma, X. Y. Zou, W. X. Jiang, and T. J. Cui, "Three-dimensional broadband and high-directivity lens antenna made of metamaterials," *J. Appl. Phys.*, Vol. 110, 044904, 2011.
49. Born, M. and E. Wolf, *Principles of Optics*, Cambridge University Press, Cambridge, 1999.
50. Pendry, J. B., "Negative refraction makes a perfect lens," *Phys. Rev. Lett.*, Vol. 85, 3966, 2000.
51. Veselago, V. G., "The electrodynamics of substances with simultaneously negative values of ε and μ," *Sov. Phys. Usp.*, Vol. 10, 509, 1968.
52. Kildishev, A. V. and V. M. Shalaev, "Engineering space for light via transformation optics," *Opt. Lett.*, Vol. 33, 43, 2008.
53. Tsang, M. and D. Psaltis, "Magnifying perfect lens and superlens design by coordinate transformation," *Phys. Rev. B*, Vol. 77, 035122, 2008.
54. Fang, N., H. Lee, C. Sun, and X. Zhang, "Sub-diffraction-limited optical imaging with a silver superlens," *Science*, Vol. 308, 534, 2005.
55. Taubner, T., D. Korobkin, Y. Urzhumov, G. Shvets, and R. Hillenbrand, "Near-field microscopy through a SiC superlens," *Science*, Vol. 313, 1595, 2006.
56. Zhang, X. and Z. W. Liu, "Superlenses to overcome the diffraction limit," *Nat. Mater.*, Vol. 7, 435, 2008.
57. Liu, Z. W., S. Durant, H. Lee, Y. Pikus, N. Fang, Y. Xiong, C. Sun, and X. Zhang, "Far field optical superlens," *Nano Lett.*, Vol. 7, 403, 2007.
58. Jacob, Z., L. V. Alekseyev, and E. Narimanov, "Optical hyperlens: Far-field imaging beyond the diffraction limit," *Opt. Express*, Vol. 14, 8247, 2006.
59. Salandrino, A. and N. Engheta, "Far-field subdiffraction optical microscopy using metamaterial crystals: Theory and simulations," *Phys. Rev. B*, Vol. 74, 075103, 2006.
60. Smolyaninov, I. I., Y. J. Huang, and C. C. Davis, "Magnifying superlens in the visible frequency range," *Science*, Vol. 315, 1699, 2007.
61. Liu, Z. W., H. Lee, Y. Xiong, C. Sun, and X. Zhang, "Optical hyperlens magnifying sub-diffraction-limited objects," *Science*, Vol. 315, 1686, 2007.
62. Rho, J., Z. Ye, Y. Xiong, X. Yin, Z. Liu, H. Choi, G. Bartal, and X. Zhang, "Spherical hyperlens for two-dimensional sub-diffractional imaging at visible frequencies," *Nat. Commun.*, Vol. 1, 143, 2010.
63. Zhang, B. L. and G. Barbastathis, "Dielectric metamaterial magnifiercreating a virtual color image withfar-field subwavelength information," *Opt. Express*, Vol. 18, 11216, 2010.
64. Jiang, W. X., C.-W. Qiu, T. C. Han, Q. Cheng, H. F. Ma, S. Zhang, and T. J. Cui, "Broadband all-dielectric magnifying lens for far-field high-resolution imaging," *Adv. Mater.*, Vol. 25, 6963–6968, 2013.
65. Mansfield, S. M. and G. S. Kino, "Solid immersion microscope," *Appl. Phys. Lett.*, Vol. 57, 2615, 1990.